INSTITUTE OF PHYSICS PUBLISHING MODELLING AND SIMULATION IN MATERIALS SCIENCE AND ENGINEERING

Modelling Simul. Mater. Sci. Eng. **12** (2004) 273–284 PII: S0965-0393(04)72862-4

Precipitation sequence in niobium-alloyed ferritic stainless steel

Nobuhiro Fujita[1], **H K D H Bhadeshia**[2] **and Masao Kikuchi**[1]

[1] Steel Research Laboratories, Nippon Steel Corporation, 20-1 Shintomi Futtsu, 293-8511, Japan
[2] Department of Materials Science and Metallurgy, University of Cambridge, Pembroke Street, Cambridge CB2 3QZ, UK

Received 11 August 2003
Published 16 February 2004
Online at stacks.iop.org/MSMSE/12/273 (DOI: 10.1088/0965-0393/12/2/008)

Abstract

Niobium is an important alloying element in the design of heat-resistant ferritic stainless steels for automotive exhaust systems. When in solid solution, it improves both the high temperature strength and the resistance to thermal fatigue. However, it also forms several kinds of precipitates during service. These reactions have been modelled, taking into account the multicomponent nature of the diffusion process and allowing for capillarity effects. It has been possible to estimate not only the volume fractions but also the particle sizes for Fe_2Nb (Laves phase) and Fe_3Nb_3C (M_6C) carbide in a 19Cr–0.8Nb steel, with good agreement against experimental data.

1. Introduction

The fuel economy of internal combustion engines and the cleanliness of the associated emissions can be improved by increasing the temperature of the exhaust gas, which currently can be in excess of 900°C. Materials are, therefore, required to resist heat and thermal fatigue, both of which are important properties for the exhaust manifold of cars.

Niobium is an important solute in the design of heat-resistant stainless steels for automotive exhaust systems [1–5]. When in solid solution, it improves both the high temperature strength and the resistance to thermal fatigue [5]. However, it also forms a variety of precipitates, including Nb(C,N) (carbonitride), Fe_2Nb (Laves phase) and Fe_3Nb_3C (M_6C carbide) during service. It is important in the development process to understand the kinetics of the simultaneous precipitation and coarsening reactions. There exists a theory for NbC formation in the austenite phase of low-alloy steels [6–10] and for precipitation sequences in ferritic, heat-resistant steels [11–15]. However, there has not been much work of this kind on ferritic stainless steels [16] because of their complexity and due to a lack of appropriate thermodynamic data. It is the purpose of this paper to model the evolution of precipitates in niobium-alloyed ferritic stainless-steels, taking into account the multicomponent nature of diffusion, of capillarity effects and of interactions between different kinds of precipitates, by using a simultaneous transformation framework [13, 14].

Table 1. Chemical composition (wt%) of the ferritic stainless steel studied here.

Steels	C	Si	Mn	Cr	Nb	N
19Cr–0.8Nb	0.014	0.2	0.3	19.6	0.78	0.016

Table 2. X-ray and chemical analyses of extraction residues from 19Cr–0.8Nb wt% steel. VW, W, S and VS stand for very weak, weak, strong and very strong x-ray intensities, respectively.

Ageing conditions		Precipitates detected			Each element in precipitates (mass%)			
Ageing temperature (˚C)	Ageing time (h)	Nb(C,N)	$M_6C : Fe_3Nb_3C$	$Fe_2M : Fe_2Nb$	Nb	Fe	Cr	N
As annealed at 1000˚C		S	VS	W	0.204	0.214	0.042	0.014
	1	VS	VS	VS	0.407	0.326	0.051	0.015
	8	S	VS	W	0.460	0.298	0.048	0.016
950	20	S	VS	W	0.458	0.289	0.047	0.016
	50	S	VS	VW	0.432	0.247	0.044	0.013
	100	VW	VS	—	0.443	0.234	0.041	0.014
1000	20	W	VS	—	0.362	0.171	0.037	0.015

2. Experimental procedure

Table 1 shows the chemical composition of niobium-alloyed ferritic stainless steel, with a nominal composition 19Cr–0.8Nb wt%. The alloy was vacuum-melted as a 10 kg ingot which was then heated to 1250˚C for 30 min in an argon atmosphere, hot-rolled to a 12 mm thickness plate and air-cooled from a finishing temperature of about 900˚C. The plate was annealed at 1000˚C for 10 min and then quenched in water. Samples were machined for a variety of isothermal heat-treatments at 950˚C and 1000˚C for up to 500 h. Electrolytically extracted residues were analysed using x-ray diffraction to identify the precipitates.

The microstructures were characterized mainly using carbon extraction replicas examined using transmission electron microscopy (TEM), electron diffraction and energy dispersive x-ray analysis (EDS). This also helped characterize particle sizes. Replicas were made by vacuum evaporating carbon films onto the sample surface. The carbon replicas were then collected on 3 mm diameter copper grids. An etching solution of $10\,g\,l^{-1}$ tetramethylammonium chloride, 10 vol% acetylacetone in methanol at a potential between 0 and 200 mV proved satisfactory during the extraction process. Because several types of precipitates are expected in aged steels, replica specimens make it easy to identify and size each phase. Thin-foil specimens can also be used but replicas are able to cover a broad size range from 10 nm to 1 μm.

M_6C type carbide may be an equilibrium phase [16, 18]; it was characterized mostly during its coarsening stage. An effective radius r was determined assuming that the area of each particle is equal to that of a circle of radius of r. At least 100 particles were measured in each experiment.

3. Experimental results

Table 2 shows the results of chemical and x-ray analyses of extracted residues from the samples aged at 950˚C and 1000˚C for a 19Cr–0.8Nb wt% steel. Nb(C,N), Laves phase (Fe_2Nb) and

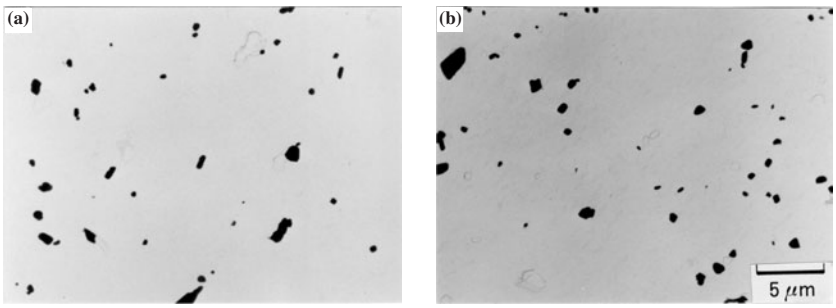

Figure 1. Transmission electron micrographs for a 19Cr–0.8Nb wt% steel aged at 950°C for (*a*) 20 h and (*b*) 100 h.

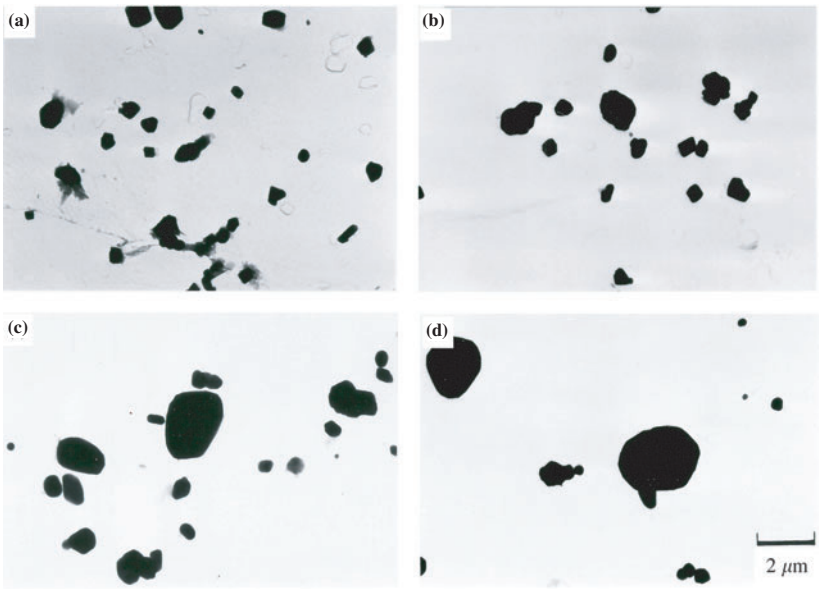

Figure 2. Extraction replica transmission electron micrographs of a 19Cr–0.8Nb wt% steel aged at 1000°C for (*a*) 1 h, (*b*) 10 h, (*c*) 100 h and (*d*) 500 h.

Fe_3Nb_3C carbide were detected during the early stages of ageing. On continued ageing, the x-ray intensity due to Nb(C,N) and Laves phase decreased and that due to Fe_3Nb_3C increased. According to a chemical analysis of the extracted residues, most of the nitrogen precipitated, probably as NbN, implying that NbC dissolves and NbN remains. The atomic ratio of Fe to Nb in the extracted residue approached unity as the ageing time increased. This indicates that the NbC and Laves phases, which contain more iron than required by stoichiometry in Fe_3Nb_3C, dissolve to give way to Fe_3Nb_3C. It appears, therefore, that the equilibrium phases in the 19Cr–0.8Nb wt% steel are NbN and Fe_3Nb_3C:

$$\alpha \rightarrow \alpha + \mathrm{Nb(C, N)} + \mathrm{Fe_2Nb} + \mathrm{Fe_3Nb_3C} \rightarrow \alpha + \mathrm{NbN} + \mathrm{Fe_3Nb_3C}$$

where α represents ferrite. Figure 1, representing specimens aged at 950°C for 20 and 100 h, shows that the precipitates are more spherical than plate or needle-shaped. Figure 2 shows transmission electron micrographs for particle coarsening as a function of ageing time. Almost

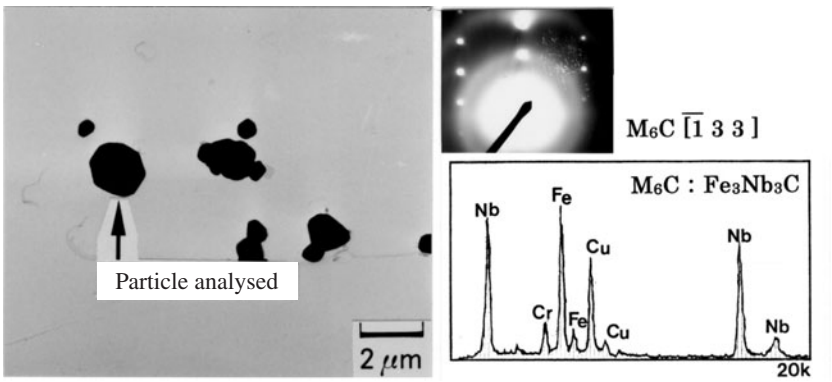

Figure 3. Transmission electron micrographs and corresponding electron diffraction and EDS data for a 19Cr–0.8Nb wt% steel aged at 1000˚C for 100 h.

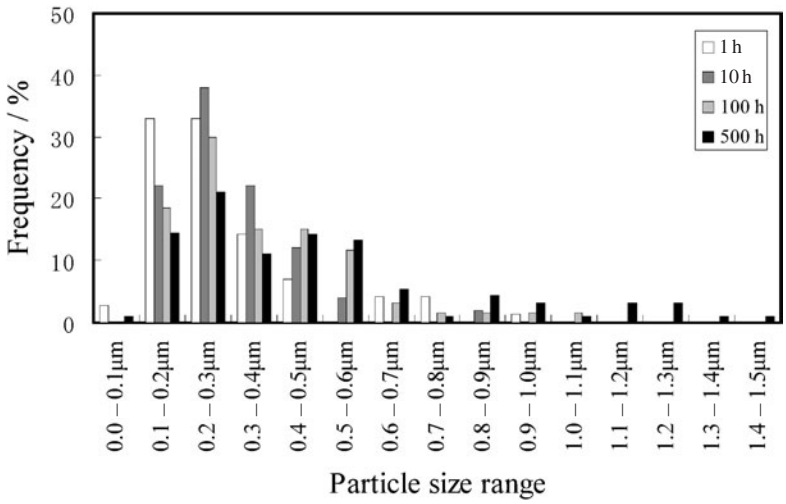

Figure 4. Changes in the particle size distribution with ageing time at 1000˚C for a 19Cr–0.8Nb wt% steel.

all of the particles following ageing at 1000˚C for 100 h were identified to be Fe_3Nb_3C (figure 3), the size distribution changing due to coarsening (figure 4).

4. Model

4.1. Nucleation

Nucleation is assumed to occur at a constant rate in the absence of soft-impingement; this is difficult to justify experimentally because of the variety of precipitation reactions that occur simultaneously. Classical nucleation theory is used to estimate the nucleation rate I for each precipitate. There are several formulae for the rate I [19–22]. For simplicity and taking into account the consumption of nucleation-sites with the term $(1 - V^{\beta}/V^{\alpha\beta})$ [10], the rate I is

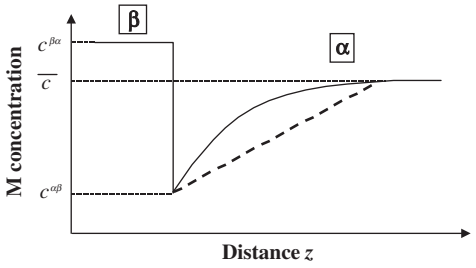

Figure 5. An illustration of the solute concentration profile during diffusion-controlled precipitation of β from α. $c^{\alpha\beta}$ and $c^{\beta\alpha}$ are concentrations at the interface α/β in the matrix α and the precipitate β, respectively.

written as

$$I = \left(1 - \frac{V^{\beta}}{V^{\alpha\beta}}\right) N_0 \frac{kT}{h} \exp\left(-\frac{G^* + Q^*}{RT}\right) \tag{1}$$

$$G^* = \frac{16\pi\sigma^3}{3\Delta G_{\mathrm{V}}^2} \tag{2}$$

where V^{β} and $V^{\alpha\beta}$ are instantaneous and equilibrium fractions of the alloy carbide, respectively, N_0 is the initial number density of nucleation sites, h and k are the Planck and Boltzmann constants, respectively, Q^* is the activation energy for the transfer of atoms across the nucleus/matrix interface, assumed to be that for volume diffusion [19], T the absolute temperature, ΔG_{V} the chemical free energy change per unit volume, σ the energy per unit area of the precipitate–matrix interface and N_0 and σ are in this paper, fitting parameters.

4.2. Growth

A reasonable approximation for isothermal diffusion-controlled growth is that the compositions of the phases in contact at the interface are locally in equilibrium. It follows that for a binary alloy these compositions are given by a tie-line of the equilibrium phase diagram. For a binary system, the tie-line is unique and passes through $\bar{c}$ which is the average concentration of solute in the alloy. The concentration profile that develops during the precipitation of a solute-rich phase such as a carbide, is illustrated in figure 5. $c^{\alpha\beta}$ is the concentration of solute in ferrite (α) which is in equilibrium with the carbide (β) and $c^{\beta\alpha}$ is the corresponding concentration in β which is in equilibrium with α. For local equilibrium to be maintained, the rate at which the solute is partitioned into the carbide must equal that at which it arrives at the interface by diffusion, giving the conservation condition

$$v(c^{\beta\alpha} - c^{\alpha\beta}) = -D \left.\frac{\partial c}{\partial z}\right|_{z=z^*} \tag{3}$$

where v is the velocity of the interface, z a co-ordinate normal to the interface, z^* the position of the interface and D is the diffusion coefficient of the solute in α. The concentration gradient is evaluated at the position of the interface, $z = z^*$. For a ternary system like Fe–M–C, the tie-line will not in general pass through $\bar{c}$ because it is necessary to simultaneously satisfy two conservation equations at the interface, one each for the substitutional element M and carbon, which diffuse at vastly different rates [23–25].

$$v(c_{\mathrm{M}}^{\beta\alpha} - c_{\mathrm{M}}^{\alpha\beta}) = -D_{\mathrm{M}} \nabla c_{\mathrm{M}} \tag{4.1}$$

$$v(c_{\mathrm{C}}^{\beta\alpha} - c_{\mathrm{C}}^{\alpha\beta}) = -D_{\mathrm{C}} \nabla c_{\mathrm{C}} \tag{4.2}$$

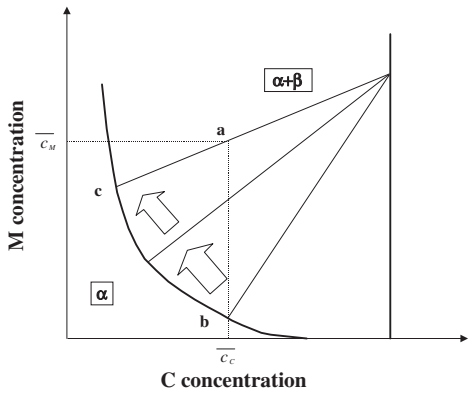

Figure 6. An illustration of an isothermal section through the Fe–M–C phase diagram, showing the precipitate (β)/ferrite (α) phase boundaries. The alloy composition is plotted as point ***a***.

In this context, the cross-diffusion effect is neglected because of the small dependence of the flux of carbon on the gradient of niobium.

According to the phase rule, there is an additional degree of freedom in a ternary alloy, making it possible to select a tie-line from the two phase $\alpha + \beta$ field, which is able to satisfy both these equations in spite of the fact that $D_{\mathrm{C}} \gg D_{\mathrm{Nb}}$, whilst at the same time maintaining local equilibrium [23–25].

There are two ways in which this can happen [23–25]. The first is for the system to choose a tie-line that greatly increases the gradient of niobium to compensate for its low diffusivity. This would require the carbide to have virtually the same niobium concentration as the matrix with very little partitioning of Nb, but with a steep concentration spike at the interface in order to maintain local equilibrium. This is only possible at large driving forces and hence is not applicable to this work.

The relevant alternative is to select a tie-line which reduces the gradient of carbon to such an extent that the flux of carbon is reduced to a level consistent with that of niobium. Referring to figure 6, the intersection of the vertical line with the $\alpha/(\alpha+\beta)$ phase field defines completely the tie-line which fixes the interface compositions in a manner which satisfies the conservation conditions because the large diffusion coefficient of carbon is compensated for by the small concentration gradient of carbon [23–25]. This assumes that the far-field concentration $\bar{c}$ does not change during transformation, i.e. there is no 'soft-impingement' of the diffusion fields of different particles. However, soft-impingement is inevitable for the later stages of transformation, in which case the tie-line controlling interface compositions must change to continue to satisfy the conservation conditions. The locus of the matrix composition due to solute depletion during precipitation is along the direction $\boldsymbol{a} \rightarrow \boldsymbol{c}$ (figure 6). The change in the matrix composition also leads to a different choice of tie-line, the locus of $c^{\alpha\beta}$ being along $\boldsymbol{b} \rightarrow \boldsymbol{c}$ (figure 6). This tie-line shifting continues until the reaction stops when the tie-line intersects the average composition $\boldsymbol{a}$ and $c^{\alpha\beta} = \boldsymbol{c}$.

The mean field approximation is used to calculate changes in $\bar{c}$ as precipitation progresses. The instantaneous value of the matrix compositions, $\bar{c}'$, is given by

$$\bar{c}' = \frac{\bar{c} - \sum_{i=1}^{n} V_i' c^{i\alpha}}{1 - \sum_{i=1}^{n} V_i'} \tag{5}$$

where V_i' is the volume fraction at any instant for the ith phase and $c^{i\alpha}$ is the equilibrium concentration in α with the ith phase. Once the interface compositions are defined as described

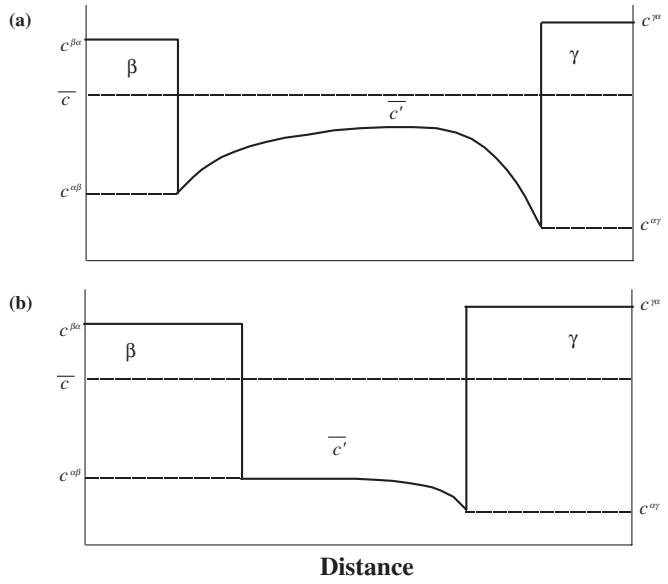

Figure 7. Distribution of solute when (*a*) both β and γ are precipitating, and (*b*) where the precipitation of β has been completed. Note that $\bar{c}'$ is the solute concentration in the matrix α.

earlier, established theory for diffusion-controlled growth can be applied to estimate the spherical particle radius r as a function of time [22, 26]:

$$z = \alpha_3\sqrt{Dt} \qquad \text{with } \alpha_3 \approx \sqrt{2\frac{\bar{c} - c^{\alpha\beta}}{c^{\beta\alpha} - \bar{c}}} \tag{6}$$

The driving force for nucleation must also be affected by soft-impingement. To deal with this, an extent of reaction parameter Φ_i is defined as follows:

$$\Phi_i = \frac{V_i'}{V^{i\alpha}} \tag{7}$$

where $V^{i\alpha}$ is the maximum fraction of the ith phase. The function Φ_i ranges from 0 to 1 and represents the fraction of excess solute remaining in the matrix relative to the equilibrium composition of the precipitate. It is assumed that the driving force for precipitation (ΔG_{V} in equation (2)) is related linearly to Φ_i:

$$\Delta G_{\mathrm{V}_i} = (1 - \Phi_i)\Delta G_{\mathrm{V}_{0i}} \tag{8}$$

where ΔG_{V_i} and $\Delta G_{\mathrm{V}_{0i}}$ are the driving forces for precipitation at an arbitrary instant and at $t = 0$, respectively.

4.3. Dissolution of the metastable phase

As mentioned in the section on soft-impingement, the mean solute concentration decreases as the reaction proceeds. Schematic composition profiles are shown in figure 7 for (*a*) at a time when both the metastable phase β and the equilibrium phase γ are precipitating in matrix α and then (*b*) when the solute concentration in the matrix reaches the equilibrium with β; precipitation of β has been completed and as γ precipitates further, removing solute, β will start to dissolve.

4.4. Capillarity

The state of equilibrium between two phases changes with the curvature of the interface separating them according to the well-established capillarity effect, which scales with the interfacial energy [22]. The free energy of a carbide phase varies relatively sharply with deviations from the stoichiometric composition so it can be assumed that the carbide composition is insensitive to the curvature. However, the equilibrium composition of the matrix changes as follows [22]:

$$c_{r,\mathrm{M}}^{\alpha\beta} = \left(1 + \frac{\sigma}{kT}\frac{v^{\beta}}{r}\frac{1 - c_{\mathrm{M}}^{\alpha\beta}}{c_{\mathrm{M}}^{\beta\alpha} - c_{\mathrm{M}}^{\beta\alpha}}\right) c_{\mathrm{M}}^{\alpha\beta} \tag{9}$$

where $c_r^{\alpha\beta}$ is the solute concentration in α which is in equilibrium with a spherical particle of β and r is the radius of curvature, which in this case also defines the particle size. The term $c^{\alpha\beta} = c_r^{\alpha\beta}$ when $r = \infty$. The modified composition $c_r^{\alpha\beta}$ is, therefore, easy to estimate for each particle. For a ternary alloy, capillarity is approximated by calculating the $\alpha/(\alpha + \beta)$ phase boundary on an isothermal section of the phase diagram, as a function of r, using equation (9). The growth velocity can then be calculated using the curvature-modified phase boundary. Particles that are smaller than the size of a critical nucleus obviously cannot grow. Nucleation occurs by random fluctuations so that the growth part in the computational scheme must start beyond the nucleation stage. Particles nucleate at different times during the course of the reaction, giving rise to a distribution of sizes.

At any given stage of precipitation, the small particles will grow at a slower rate than a larger particle because the capillarity effect reduces the supersaturation for small particles. Capillarity has the consequence that large particles have lower solute concentrations at the interface, $c_r^{\alpha\beta}$, than small particles. This drives coarsening, which becomes a natural consequence of the precipitation theory, since changes, including the dissolution of particles, continue to happen as long as there are solute concentration gradients.

5. Calculations

5.1. Parameters required for calculations

ΔG_{V}, the chemical free energy change per unit volume of precipitate, is given by

$$\Delta G_{\mathrm{V}} = \frac{\Delta G}{v^i \times V^{i\alpha}}$$

where v^i is the molar volume of the ith phase and ΔG is the molar free energy change of the precipitation reaction. ΔG can be obtained with a CALPHAD via an explicit equation [21]. There are thermodynamic data for Nb(C,N), but unfortunately not for the Laves phase and M_6C type carbide in multi-component systems of the type considered here. However, solubility products have recently been determined [18] and can be used to estimate ΔG:

$$\mathrm{Fe_2Nb}: \qquad \log[\mathrm{Nb}] = -\frac{3780.3}{T} + 2.4646$$

$$\mathrm{Fe_3Nb_3C}: \qquad \log[\mathrm{Nb}][\mathrm{C}]^3 = -\frac{11\,613}{T} + 5.2178$$

where the concentrations are in wt% and T is the absolute temperature (table 3). M_6C includes Cr and Nb (figure 3), so the diffusion of both elements needs to be considered. However, there is much more Cr than Nb in this steel and the content of Cr in M_6C is less than that of Nb (figure 3 and table 2). The similar diffusion coefficients of both these elements (Fridberg *et al* [27])

Table 3. Parameters used in the kinetic calculations of NbN, Fe_2Nb and Fe_3Nb_3C precipitation in a 19Cr–0.8Nb wt% steel and D_0 in diffusion coefficient and activation energy for diffusion of Nb and Cr in ferrite [27].

Number density of sites: N_0	
NbN (m^{-3})	2×10^{12}
Fe_2Nb (m^{-3})	3×10^{11}
Fe_3Nb_3C (m^{-3})	3×10^{12}
Interfacial energy: σ	
NbN ($J\,m^{-2}$)	0.230
Fe_2Nb ($J\,m^{-2}$)	0.280
Fe_3Nb_3C ($J\,m^{-2}$)	0.330
D_0 in diffusion coefficent of Nb in ferrite ($m^2\,s^{-1}$)	1.3×10^{-4}
Activation energy for diffusion of Nb in ferrite: Q ($J\,mol^{-1}$)	240×10^3
D_0 in diffusion coefficent of Cr in ferrite ($m^2\,s^{-1}$)	1.5×10^{-4}
Activation energy for diffusion of Cr in ferrite: Q ($J\,mol^{-1}$)	240×10^3

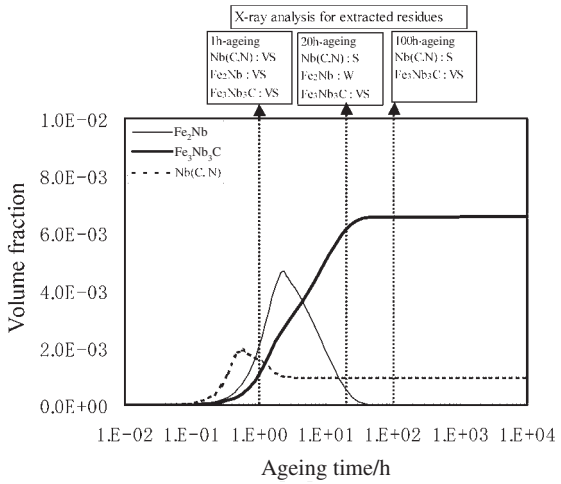

Figure 8. Calculations of multiple precipitation reactions for a 19Cr–0.8Nb wt% steel aged at 950°C.

are shown in table 3. Bearing these observations in mind, the calculations have been carried out assuming that the precipitation proceeds in a Fe–Nb–C system. There are two unknown parameters, the number density of nucleation sites N_0 and the interfacial energy σ. They are treated as fitting parameters. The sensitivity of the results to these fitting parameters has been in the context of M_6C precipitation in a niobium-alloyed ferritic stainless steel and that on the NbC in austenite has been reported [10, 16]. It is found that the results are affected more by the interfacial energy than the number density. For example, an order of magnitude increase in N_0 leads to an approximately 20% decrease in mean particle size and a corresponding increase in σ leads to approximately a three fold increase in mean particle size. The parameters in this paper were chosen to obtain a reasonable agreement with experiments.

5.2. Volume fraction

Calculated volume fractions for each phase at 950°C are shown in figure 8 along with the experimental observations. The model is able to correctly estimate the precipitation sequence.

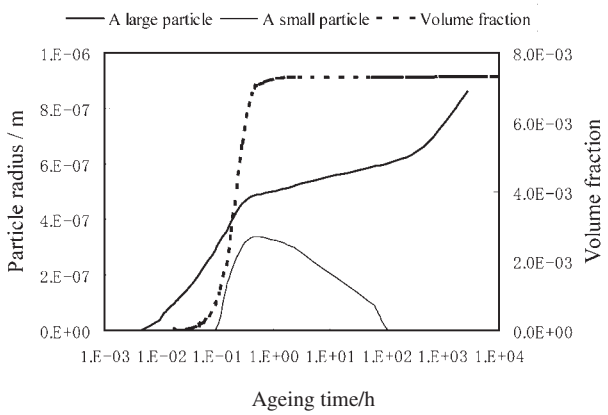

Figure 9. Calculated data on the volume fraction and particle radius changes for Fe_3Nb_3C at 1000°C in a 19Cr–0.8Nb wt% steel with $N_0 = 3 \times 10^{12}\,m^{-3}$ and $\sigma = 0.33\,J\,m^{-2}$.

5.3. Particle size

Figure 9 shows the calculation results indicating how the particle radius and volume fraction of Fe_3Nb_3C which can be assumed to be an equilibrium phase changes with ageing time at 1000°C. As expected, a large particle, which nucleated early, grows continuously even as the volume fraction approaches equilibrium. However, because of the capillarity effect, the small particle which nucleated late begins to dissolve even as the large one grows. Figure 10 shows the changes in volume fraction, mean particle radius and number density with ageing time at 1000°C and the experimental data of the mean particle radii for Fe_3Nb_3C.

The measured mean radii remain level until 100 h followed by a gradual increase. As shown in figure 4, the frequency of large particles increases and that of small particles decreases after 100 h ageing. After a stasis region where the number density does not change, coarsening occurs, where the mean particle radius tends to change in proportion to $\frac{1}{3}$. This is described as Ostwald ripening [28]. In the stasis region, some particles begin to dissolve, as is also evident from the plots shown in figure 9. However, most of the particles nucleate early so it takes considerable time for the smaller amongst them to dissolve, given that this coarsening phenomenon is driven by small capillarity-induced concentration gradients.

Although the experimental data are not in the parabolic growth stage but in the stasis and coarsening regions, the calculated kinetics compare well with experiments. The calculations represent the whole of the precipitation process from nucleation to coarsening of Fe_3Nb_3C carbide, which is assumed to be the equilibrium phase. One computational problem with calculations of this kind is that the timescales associated with the precipitation and with the coarsening stages are large. Caution must, therefore, be exercised to avoid the accumulation of numerical errors. The computational time steps were chosen to avoid these difficulties without making the calculation time unbearable. The other reason for discrepancy between calculations and experiments is the interfacial energy. The values must, in principle, change with coherency [9].

6. Summary

A methodology has been developed to deal with the nucleation and growth of spherical precipitates of multiple precipitation reactions, Nb(C,N), Laves phase and M_6C in

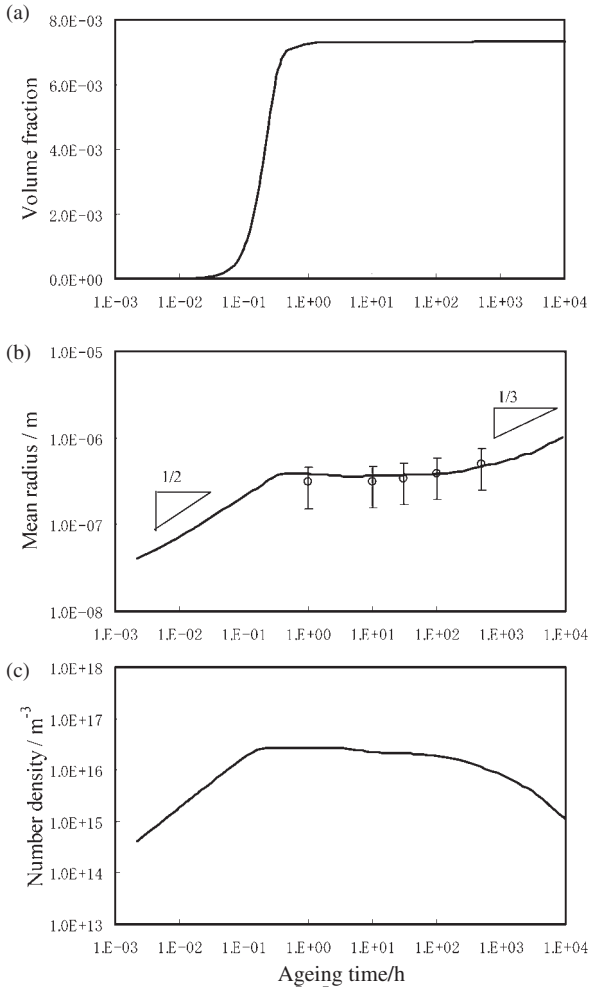

Figure 10. Changes of (*a*) volume fraction, (*b*) mean particle size and (*c*) number density of Fe_3Nb_3C with ageing time at 1000˚C for a 19Cr–0.8Nb wt% steel.

niobium-alloyed ferritic stainless steels of the type used to manufacture automobile exhaust manifolds. The method includes capillarity and so allows the simulation of the whole precipitation process from nucleation to coarsening for an equilibrium phase. Choosing two adjustable parameters, i.e. the number density of nucleation sites and the interfacial energy, the calculations showed good agreement with experimental measurements of both volume fraction and particle size.

References

[1] Nakamura S, Miyagusu K and Uematsu Y 1991 *CAMP-ISIJ* **4** 1788
[2] Ohmura K, Fujita N, Kikuchi M, Suzuki T and Hiroshige I 1991 *CAMP-ISIJ* **4** 1796
[3] Miyazaki A, Gunzi M and Yoshioka K 1993 *Kawasaki Steel Giho.* **25** 112
[4] Akiyama S 1991 *Nippon Stainless Tech. Rep.* **26** 57
[5] Fujita N, Ohmura K, Kikuchi M, Suzuki T, Funaki S and Hiroshige I 1996 *Scr. Mater.* **35** 705

[6] Dutta B and Sellars M 1987 *Mater. Sci. Technol.* **3** 197
[7] Saito Y, Shiga C and Enami T 1988 *Proc. Int. Conf. on Physical Metallurgy of Thermomechanical Processing of Steels and Other Metals* ed I Tamura (Tokyo: ISIJ) p 753
[8] Akamatsu S, Matsumura Y, Senuma T, Yada H and Ishikawa S 1989 *Tetsu-to-Hagane* **75** 933
[9] Okamoto R and Suehiro M 1998 *Tetsu-to-Hagane* **84** 650
[10] Fujita N and Bhadeshia H K D H 2001 *Mater. Sci. Technol.* **17** 403
[11] Baker R G and Nutting J 1959 *J. Iron Steel Inst.* **192** 257
[12] Thomson R C and Bhadeshia H K D H 1994 *Mater. Sci. Technol.* **10** 193
[13] Robson J D and Bhadeshia H K D H 1997 *Mater. Sci. Technol.* **13** 631
[14] Fujita N and Bhadeshia H K D H 2002 *ISIJ Int.* **42** 760
[15] Robson J D and Bhadeshia H K D H 1996 *CALPHAD* **20** 447
[16] Fujita N, Bhadeshia H K D H and Kikuchi M 2002 *Metall. Mater. Trans* A **33** 3339
[17] Ashby M F and Ebeking R 1966 *Trans. TMS-AIME* **236** 1396
[18] Fujita N, Kikuchi M and Ohmura K 2003 *ISIJ Int.* **43** 1999 accepted
[19] Turnbull D and Fisher J C 1949 *J. Chem. Phys.* **17** 71
[20] Russell K C 1968 Phase transformations *ASM Seminar* p 219
[21] Russell K C 1980 *Adv. Colloid Interface Sci.* **13** 205
[22] Christian J W 2001 *Theory of Transformations in Metals and Alloys* 3rd edn (part 1) (Oxford: Pergamon)
[23] Coates D E 1973 *Metall. Trans.* A **4** 2313
[24] Kirkaldy J S 1958 *Can. J. Phys.* **36** 907
[25] Bhadeshia H K D H 1985 *Prog. Mater. Sci.* **29** 321
[26] Zener C 1949 *J. Appl. Phys.* **20** 950
[27] Fridberg J, Torndahl L-E and Hillert M 1969 *Jernkotorets Ann.* **153** 263
[28] Lifshitz I M and Slyozov V V 1961 *J. Phys. Chem. Solids* **19** 35